Wave Motion 69 (2017) 35–49

Contents lists available at ScienceDirect

Wave Motion

journal homepage: www.elsevier.com/locate/wavemoti

# Dynamic homogenisation of Maxwell's equations with applications to photonic crystals and localised waveforms on gratings

B. Maling [a], D.J. Colquitt [b], R.V. Craster [a,*]

[a] Department of Mathematics, Imperial College London, London, SW7 2AZ, UK
[b] Department of Mathematical Sciences, University of Liverpool, Liverpool, L69 7BX, UK

ARTICLE INFO

*Article history:*
Received 8 November 2015
Received in revised form 30 October 2016
Accepted 1 November 2016
Available online 10 November 2016

*Keywords:*
Asymptotics
Homogenisation
Bloch waves
Electromagnetism
Grating
Photonic crystal

ABSTRACT

A two-scale asymptotic theory is developed to generate continuum equations that model the macroscopic behaviour of electromagnetic waves in periodic photonic structures when the wavelength is not necessarily long relative to the periodic cell dimensions; potentially highly-oscillatory short-scale detail is encapsulated through integrated quantities. The resulting equations include tensors that represent effective refractive indices near band edge frequencies along all principal axes directions, and these govern scalar functions providing long-scale modulation of short-scale Bloch eigenstates, which can be used to predict the propagation of waves at frequencies outside of the long wavelength regime; these results are outside of the remit of typical homogenisation schemes.

The theory we develop is applied to two topical examples, the first being the case of aligned dielectric cylinders, which has great importance in modelling photonic crystal fibres. Results of the asymptotic theory are verified against numerical simulations by comparing photonic band diagrams and evanescent decay rates for guided modes. The second example is the propagation of electromagnetic waves localised within a planar array of dielectric spheres; at certain frequencies strongly directional propagation is observed, commonly described as dynamic anisotropy. Computationally this is a challenging three-dimensional calculation, which we perform, and then demonstrate that the asymptotic theory captures the effect, giving highly accurate qualitative and quantitative comparisons as well as providing interpretation for the underlying change from elliptic to hyperbolic behaviour.



## 1. Introduction

Theoretical and practical developments in the field of metamaterials, motivated by the work of Veselago [1] and later Pendry [2], have led to a substantial literature on the asymptotic homogenisation of Maxwell's equations in composite media [3–8]. The effective medium models obtained from the multiple-scale methods used in these articles are broader in scope than those given by the electromagnetic mixing formulae of Maxwell–Garnett, Bruggeman and others [9], but like these they are limited to the static or quasi-static regime in which it is assumed that the wavelength is much greater than the size in the repeating cell of the composite. A special class of two-dimensional metamaterial may be referred

* Corresponding author.
*E-mail address:* r.craster@imperial.ac.uk (R.V. Craster).

http://dx.doi.org/10.1016/j.wavemoti.2016.11.003

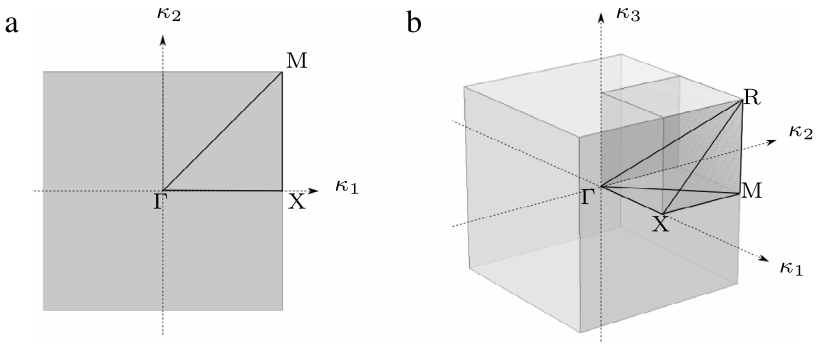


**Fig. 1.** First Brillouin zones for (a) simple square and (b) simple cubic arrays. The triangle in (a), or tetrahedron of (b), whose vertices are labelled are the *irreducible* Brillouin zones, defined as the first Brillouin zones reduced by the point symmetries of the cell, in this case that of the square, cube respectively. Standing waves occur at each of the lettered points.

to as a metasurface [10,11], or in the case of a two-dimensional array of scatterers, a metafilm [12]. The application of homogenisation in these cases gives rise to generalised boundary conditions [13], which are similarly found at the surfaces of composite materials [14], or on conducting surfaces with periodic corrugations [15,16].

Alongside metamaterials, the rich band structures possessed by photonic crystals (PCs) that are typically formed from periodic dielectric structures [17], give rise to a host of novel physical phenomena. Such effects, including light confinement [18], dynamic anisotropy [19], and ultrarefraction [20,21], are associated with high-frequency bands, and hence the long-wavelength assumption associated with effective medium models does not hold. As a result, traditional homogenisation theories are not applicable in this regime; instead, full-wave simulations, usually based on the finite element method (FEM), are deemed necessary to solve scattering problems under such conditions. The computational cost of solving these problems increases rapidly with the number of nodes, which is intimately connected with the dimensionality and scale of the system, as well as the wavelength within the constitutive materials. This can become prohibitive especially in the case of large three-dimensional structures. On the other hand, propagating fields in the bulk of a photonic crystal are naturally expressed in terms of Bloch waves, and the associated Bloch eigenvalue problem can be solved with relative ease using an FEM solver or alternatively using plane-wave expansion methods [22].

In this paper, we develop a complementary approach for studying the propagation of waves in periodic photonic structures in the high-frequency regime. Adopting a two-scale approach not dissimilar to those used in classical homogenisation theories, we are led to a hierarchy of equations that are solved on the cell level, and from these we derive long-scale PDEs that govern the modulation of rapidly-oscillating Bloch eigenstates of the structure. Our approach differs fundamentally from classical homogenisation theories which assume that the wavelength is long compared with the size of the repeating cell, whereas we require that the operating frequency is close to a standing wave eigenfrequency of the structure, and in this regime a dynamic long-scale emerges as the Bloch wavelength of the propagating field. The method is based on high-frequency homogenisation (HFH), developed in the article [23], in which a similar analysis was performed for periodic structures governed by the planar Helmholtz equation. Further work has been done to extend the theory to in-plane elasticity [24–26], and the main result of this paper is to extend the theory to the three-dimensional vector formulation of Maxwell's equations. As a result, we recover tensors that represent effective refractive indices near band edge frequencies along all principal axes directions, rather than effective $\varepsilon$ and $\mu$ tensors. The only case in which the latter can be recovered is the low-frequency quasi-static limit, which we do not pursue here as this has been done before by various authors. However, we do show that in the commonly-occurring case of purely dielectric media, the system of equations garnered from the HFH methodology in the low-frequency limit can be written in the form of classical homogenisation theories, from which an effective permittivity tensor $\varepsilon^{\text{hom}}$ can be extracted; this is left to Appendix C.

In order to demonstrate the efficacy of the asymptotic method developed herein, we consider two topical examples: the first is that of a dielectric structure that is invariant in one spatial direction and periodic in the remaining two; such structures are typical models for photonic crystal fibres (PCFs) [27]. Compared with fully three-dimensional problems, this example has the advantage that the dependence of the field on the third spatial coordinate, say $x_3$, can be explicitly factored out as being proportional to $\exp(i\beta x_3)$, reducing the problem to a quasi-two-dimensional one (see Fig. 5), and is therefore useful for testing the theory in a regime where full numerical simulations are tractable. Specifically, we consider the prototypical example of dielectric cylinders embedded in a homogeneous background, previously studied in the articles [28,29].

The second application we choose is that of guided waves within a two-dimensional array of dielectric spheres. Waves of this type exhibit Bloch quasi-periodicity in the array and decay exponentially with perpendicular distance from the array; similar waves in other physical systems have been described as Rayleigh–Bloch surface waves [30,26] or array-guided surface waves [31,32], and have been examined for dielectric spheres in linear arrays [33], as well as planar arrays [34,35], but here we focus attention on dynamic in-plane effects, which have previously not been studied in this context. Using the asymptotic method developed herein, we identify frequencies for which marked dynamic anisotropy occurs; this effect is encapsulated by a locally hyperbolic partial differential operator. The effect leads to striking field patterns when a

source is placed within the planar array of spheres, and for the vector Maxwell system the three-dimensional simulations used to solve this problem are substantial and require many hours of computer time. The asymptotic method, on the other hand, provides quantitatively comparable results, as well as providing physical insight. We note that while under some circumstances the planar array could be described as a metasurface, we are working in the high-frequency regime, and the necessary conditions for classical homogenisation are not satisfied. In this context, the structure is therefore better described as a grating, or planar photonic crystal.

The article is structured as follows: in Section 2 we introduce the governing equations and clarify necessary details regarding periodicity through reciprocal lattices, Brillouin zones and Bloch waves. Given these preliminaries we develop the asymptotic theory in Section 3, and use this as an opportunity to clarify some details regarding Dirac-like points (Section 3.2). Applications to PCFs and then to array-guided surface waves are given in Sections 4 and 5 respectively, in which we use the asymptotic theory to complement full numerical simulations. Some concluding remarks are drawn together in Section 6.

## 2. Governing equations and reciprocal lattice

For time-harmonic excitations proportional to $\exp(-i\omega t)$, and in the absence of sources, Maxwell's equations in magneto-dielectric media are given by:

$$\begin{aligned} \nabla\cdot\mathbf{D} &= 0, \qquad \nabla\times\mathbf{E}-i\omega\mathbf{B}=0,\\ \nabla\cdot\mathbf{B} &= 0, \qquad \nabla\times\mathbf{H}+i\omega\mathbf{D}=0, \end{aligned} \tag{1}$$

where $\mathbf{E}$ and $\mathbf{B}$ are the electric and magnetic fields respectively and are related to the displacement field $\mathbf{D}$ and magnetising field $\mathbf{H}$ through the constitutive relations

$$\mathbf{D}=\varepsilon\mathbf{E}, \qquad \mathbf{B}=\mu\mathbf{H}. \tag{2}$$

The permittivity $\varepsilon = \varepsilon_r\varepsilon_0$ and permeability $\mu = \mu_r\mu_0$ are assumed to be piecewise smooth, scalar functions. Our convention is to assume that the fields are complex vectors in $\mathbb{C}^3$ and the measurable fields are obtained by taking the real part. Combining the curl equations in (1) with the constitutive relations (2) yields a decoupled equation satisfied by the magnetising field:

$$-\nabla\times\varepsilon^{-1}(\mathbf{x})\nabla\times\mathbf{H}(\mathbf{x})+\mu(\mathbf{x})\omega^2\mathbf{H}(\mathbf{x})=0, \tag{3}$$

along with the condition that the component of both $\mathbf{E}$ and $\mathbf{H}$ parallel to a discontinuity in $\varepsilon$ or $\mu$ must be continuous. In practice, both $\varepsilon$ and $\mu$ are usually piecewise constant, and (3) reduces to the vector Helmholtz equation. Perfect conductors can also be included in the structure, which impose a vanishing component of $\mathbf{E}$ parallel to the boundary.

For the sake of simplicity, we assume that the underlying periodicity of the structure is that of a simple cubic array. However, we remark that the approach developed here can easily be generalised to other lattice structures. We introduce a Cartesian co-ordinate system with basis vectors $\hat{\mathbf{x}}_i$ for $i=1,2,3$ and demand

$$\varepsilon(\mathbf{x})=\varepsilon(\mathbf{x}+2l[m\hat{\mathbf{x}}_1+n\hat{\mathbf{x}}_2+p\hat{\mathbf{x}}_3]), \qquad \mu(\mathbf{x})=\mu(\mathbf{x}+2l[m\hat{\mathbf{x}}_1+n\hat{\mathbf{x}}_2+p\hat{\mathbf{x}}_3]), \tag{4}$$

for $m,n,p\in\mathbb{Z}$. The primitive lattice vectors $2l\{\hat{\mathbf{x}}_i\}$ form an orthonormal set, and the elementary cell $\mathcal{C}$ can be chosen as any cube of side $2l$ oriented in accordance with these. Also central to our analysis will be the first Brillouin zone, defined in terms of the reciprocal lattice vectors $\mathbf{k}_i$ for $i=1,2,3$, where $\mathbf{k}_i\cdot 2l\hat{\mathbf{x}}_j=2\pi\delta_{ij}$.

The relevance of reciprocal space stems from Bloch's theorem, which states that for an infinite structure with direct lattice vectors $\{\mathbf{d}\}$, the field components are quasi-periodic such that $\mathbf{H}(\mathbf{x}+\mathbf{d})=\mathbf{H}(\mathbf{x})\exp(i\mathbf{k}\cdot\mathbf{d})$, and similarly for $\mathbf{E}$, where in this context the reciprocal vector $\mathbf{k}$ is called the Bloch wave vector. In particular, if the Bloch wave vector corresponds to a reciprocal lattice vector, the field has the periodicity of the direct lattice, resulting in a standing wave solution. Standing wave solutions are found whenever the Bloch wave vector implies periodicity or anti-periodicity in each spatial direction; these standing wave points will be critical to our analysis, and are labelled as in Fig. 1 for convenience.

## 3. The asymptotic procedure

To adopt a two-scale approach we define the periodic micro-scale position vector $\boldsymbol{\xi}=(\mathbf{x}-\mathbf{x}_\mathbf{c})/l$, where $\mathbf{x}_\mathbf{c}$ is the centre of a chosen cell $\mathcal{C}$, and hence $\xi_i\in[-1,1]$ for $i=1,2,3$ when $\boldsymbol{\xi}\in\mathcal{C}$. From Bloch theory, we know that the three-dimensional structure admits standing wave solutions at discrete eigenfrequencies, corresponding to solutions with Bloch wave vectors at the vertices of the first Brillouin zone. Perturbing the frequency slightly from these standing wave frequencies results in long wavelength modulation of the Bloch eigenstates, and with this in mind we introduce a dynamic macro-scale position vector $\mathbf{X}=\eta\mathbf{x}/l$, with $0<\eta\ll 1$. Assuming there is a natural separation of scales $\mathbf{X}$ will encode the long-scale response of the structure, in what follows we study the asymptotic behaviour of the modes in the vanishing limit of $\eta$ (see Fig. 2).

As is typical in homogenisation theories, the disparity of the length scales associated with $\boldsymbol{\xi}$ and $\mathbf{X}$ allows us to treat them as independent variables, so the partial derivative operators are expanded using the chain rule as

$$\frac{\partial}{\partial x_i}=\frac{1}{l}\left(\frac{\partial}{\partial\xi_i}+\eta\frac{\partial}{\partial X_i}\right), \tag{5}$$

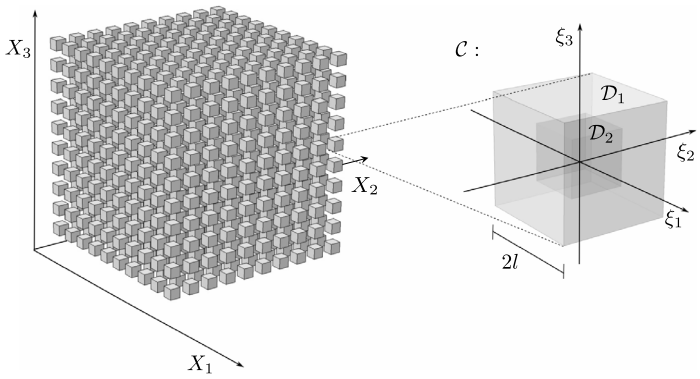


**Fig. 2.** Disparate co-ordinate systems in a two-phase triply-periodic structure. The micro-scale co-ordinates $(\xi_1, \xi_2, \xi_3)$ capture the field variation over a single elementary cell $\mathcal{C} = \mathcal{D}_1 \cup \mathcal{D}_2$, whilst the macro-scale co-ordinates $(X_1, X_2, X_3)$ encode the long-scale behaviour of the medium over multiple cells.

for $i = 1, 2, 3$. We stress that the separation of scales is an assumption, rather than a result of the theory, and for practical purposes its validity is verified a posteriori; we simply assume that the frequency of excitation is close enough to the chosen eigenfrequency for the scale-separation assumption to hold. The field is hence considered a function of both independent variables, so (3) is expanded in terms of dimensionless quantities as

$$-(\nabla_\xi + \eta\nabla_X) \times \varepsilon_r^{-1}(\boldsymbol{\xi})(\nabla_\xi + \eta\nabla_X) \times \mathbf{H}(\boldsymbol{\xi}, \mathbf{X}) + \mu_r(\boldsymbol{\xi})\Omega^2\mathbf{H}(\boldsymbol{\xi}, \mathbf{X}) = 0, \tag{6}$$

where $\Omega = \omega l/c$ and $c = 1/\sqrt{\varepsilon_0\mu_0}$ is the vacuum speed of light. The continuity conditions at phase interfaces are given in terms of the magnetic field as

$$\mathbf{n} \times \Big[\mathbf{H}(\boldsymbol{\xi}, \mathbf{X})\Big]_{\partial\mathcal{D}_{1,2}} = 0, \qquad \mathbf{n} \times \Big[\varepsilon_r^{-1}(\boldsymbol{\xi})(\nabla_\xi + \eta\nabla_X) \times \mathbf{H}(\boldsymbol{\xi}, \mathbf{X})\Big]_{\partial\mathcal{D}_{1,2}} = 0, \tag{7}$$

where $[\cdot]$ denotes a jump discontinuity and $\mathbf{n}$ is normal to the interface $\partial\mathcal{D}_{1,2}$ between two adjacent phases. We seek solutions to (6) and (7) in the form of the following ansätzes using the small parameter $\eta$:

$$\mathbf{H} = \sum_{i=0}^{\infty} \eta^i \mathbf{H}_i, \qquad \Omega^2 = \sum_{i=0}^{\infty} \eta^i \Omega_i^2, \tag{8}$$

and periodic/antiperiodic conditions are to be set in the short scale, thus restricting attention to the Γ, X, M and R points. This leads to a hierarchy of equations to be solved systematically from the lowest order in $\eta$. The leading order system poses an eigenvalue problem for a standing wave solution of the periodic Maxwell system:

$$-\nabla_\xi \times \varepsilon_{\mathrm{r}}^{-1}(\boldsymbol{\xi})\nabla_\xi \times \mathbf{H}_0(\boldsymbol{\xi}, \mathbf{X}) + \mu_{\mathrm{r}}(\boldsymbol{\xi})\Omega_0^2\mathbf{H}_0(\boldsymbol{\xi}, \mathbf{X}) = 0, \tag{9}$$

subject to continuity conditions

$$\mathbf{n} \times \Big[\mathbf{H}_0(\boldsymbol{\xi}, \mathbf{X})\Big]_{\partial\mathcal{D}_{1,2}} = 0, \qquad \mathbf{n} \times \Big[\varepsilon_r^{-1}(\boldsymbol{\xi})\nabla_\xi \times \mathbf{H}_0(\boldsymbol{\xi}, \mathbf{X})\Big]_{\partial\mathcal{D}_{1,2}} = 0. \tag{10}$$

Since the operator and boundary conditions depend only on the short-scale, this problem can be solved on the cell level. The general solution is then a linear combination of the independent vector solutions, whose coefficients must be allowed to vary on the long-scale. Explicitly we have

$$\mathbf{H}_0(\mathbf{X}, \boldsymbol{\xi}) = f_0^{(r)}(\mathbf{X})\mathbf{h}_0^{(r)}(\boldsymbol{\xi}, \Omega_0), \tag{11}$$

where we sum over the repeated index $r = 1, 2, \ldots, p$ for an eigenvalue with multiplicity $p$. Each term is the product of an unknown long-scale scalar function $f_0^{(r)}(\mathbf{X})$ with a known short-scale vector function $\mathbf{h}_0^{(r)}(\boldsymbol{\xi}, \Omega_0)$, which is a Bloch eigensolution of (9). The main aim of the asymptotic method is to find PDEs satisfied by the long-scale functions. It will be useful to introduce the electric field eigensolutions

$$\mathbf{e_0}^{(n)} = \frac{i}{\Omega_0}\varepsilon_{\mathrm{r}}^{-1}\nabla_\xi \times \mathbf{h}_0^{(n)}, \tag{12}$$

which are also modulated by the long-scale functions appearing in (11). Note that the separated-scale solutions are distinguished by lower-case lettering; this convention is followed for the remainder of the paper.

Having solved the leading order system, we move on to the next order in the hierarchy, resulting in an inhomogeneous system:

$$-\nabla_\xi \times \varepsilon_{\mathrm{r}}^{-1}\nabla_\xi \times \mathbf{H}_1 + \mu_{\mathrm{r}}\Omega_0^2\mathbf{H}_1 = \nabla_\xi \times \varepsilon_{\mathrm{r}}^{-1}\nabla_X \times \mathbf{H}_0 + \varepsilon_{\mathrm{r}}^{-1}\nabla_X \times \nabla_\xi \times \mathbf{H}_0 - \mu_{\mathrm{r}}\Omega_1^2\mathbf{H}_0, \tag{13}$$

subject to jump discontinuity conditions:

$$\mathbf{n} \times \left[\mathbf{H}_1\right]_{\partial \mathcal{D}_{1,2}} = 0, \qquad \mathbf{n} \times \left[\varepsilon_r^{-1}\left(\nabla_\xi \times \mathbf{H}_1 + \nabla_X \times \mathbf{H}_0\right)\right]_{\partial \mathcal{D}_{1,2}} = 0. \tag{14}$$

Before attempting to solve this, we derive a compatibility condition (see Appendix A), whose implication depends on the nature of the eigenvalue in question. In every case, the result is the following equation, posed in the long scale:

$$P_j^{nr} \frac{\partial f_0^{(r)}}{\partial X_j} + \Omega_1^2 Q^{nr} f_0^{(r)} = 0, \tag{15}$$

where

$$P_j^{nr} = i\Omega_0 \int_C \left\{\mathbf{e_0}^{(n)*} \times \mathbf{h}_0^{(r)} + \mathbf{e_0}^{(r)} \times \mathbf{h}_0^{(n)*}\right\}_j \mathrm{d}V, \qquad Q^{nr} = \int_C \mu_r \mathbf{h}_0^{(n)*} \cdot \mathbf{h}_0^{(r)} \mathrm{d}V,$$

and we sum over the repeated indices $j$ and $r$. There is a physical interpretation: For fixed $n$, with $r = n$, the components of $P_j^{nn}$ form the integrated real part of the time-averaged Poynting flux $\mathbf{e_0}^{(n)} \times \mathbf{h}_0^{(n)*}$ over the cell, while $Q^{nn}$ is the electromagnetic energy within the cell; their ratio is the group velocity, which is zero for standing wave solutions.

Two situations occur, depending on whether the components of $P_j^{nr}$ are all zero or not. In most cases the components are all zero implying that $\Omega_1 = 0$, and we must proceed further up the asymptotic hierarchy; we treat this in Section 3.1. If, however, $P_j^{nr}$ has non-zero components, Eq. (15) governs the long-scale envelope functions in (11) to leading order. This implies linear dispersion, which is a feature of so-called Dirac-like points [36], and we consider these in Section 3.2.

There is a further subtlety associated with the components. If $n \neq r$ then the components of $P_j^{nr}$ can be made to be zero either by geometry or through changes in material parameters; this is called degeneracy: the first and most frequent type encountered is an *essential* degeneracy, which results from the invariance of the system under a particular symmetry transformation. For cubic and square arrays, such degeneracies can be shown by symmetry to yield $P_j^{nr} = 0$. The second case is that of an *accidental* degeneracy, which occurs if we continuously tune the parameters of the structure until two or more otherwise distinct eigenvalues occur at the same frequency. Such degeneracies do not result directly from symmetry, and in general $P_j^{nr} \neq 0$ for $n \neq r$; we treat both types.

### 3.1. Distinct eigenvalues/essential degeneracies: quadratic dispersion

We deduce from (15) that if $P_j^{nr} = 0$ for all permutations of indices, then $\Omega_1 = 0$ for non-trivial solutions. In this case it is necessary to advance further up the asymptotic hierarchy to find the PDEs satisfied by the long-scale functions in (11). In such cases, the solution to (13) consists of a complimentary part, which has the same short scale form as the leading order solution, and a particular solution modulated by partial derivatives of $f_0$. The most general form thus has components given by

$$H_{1i}(\mathbf{X}, \boldsymbol{\xi}) = f_1^{(r)}(\mathbf{X}) h_{0i}^{(r)}(\boldsymbol{\xi}, \Omega_0) + f_{0,X_j}^{(r)}(\mathbf{X}) h_{1ij}^{(r)}(\boldsymbol{\xi}, \Omega_0), \tag{16}$$

for $i = 1, 2, 3$ and we sum over repeated indices $j$ and $r$. Exploiting the linearity of the system and the independence of the disparate position variables, (13) separates to $3p$ systems of 3 coupled scalar equations corresponding to each permutation of $j, r$. The solution hence contains a further $9p$ known short-scale functions (the components of $h_{1ij}^{(r)}$), along with another $p$ unknown long-scale functions $f_1^{(r)}$.

We advance to $\mathcal{O}(\eta^2)$, which yields a second inhomogeneous system:

$$\begin{aligned} -\nabla_\xi \times \varepsilon_r^{-1} \nabla_\xi \times \mathbf{H}_2 + \mu_r \Omega_0^2 \mathbf{H}_2 = {} & \nabla_\xi \times \varepsilon_r^{-1} \nabla_X \times \mathbf{H}_1 \\ & + \varepsilon_r^{-1} \nabla_X \times \nabla_\xi \times \mathbf{H}_1 + \varepsilon_r^{-1} \nabla_X \times \nabla_X \times \mathbf{H}_0 - \mu_r \Omega_2^2 \mathbf{H}_0, \end{aligned} \tag{17}$$

subject to jump discontinuity conditions

$$\mathbf{n} \times \left[\mathbf{H}_2\right]_{\partial \mathcal{D}_{1,2}} = 0, \qquad \mathbf{n} \times \left[\varepsilon_r^{-1}\left(\nabla_\xi \times \mathbf{H}_2 + \nabla_X \times \mathbf{H}_1\right)\right]_{\partial \mathcal{D}_{1,2}} = 0. \tag{18}$$

In Appendix B we derive a second compatibility condition that is analogous to Eq. (15). The result is a system of PDEs satisfied by the modulation functions $f_0^{(n)}(\mathbf{X})$, posed on the long-scale only. After diagonalisation (see Appendix B), we have uncoupled equations of the form

$$T_{ij}^{nn} \frac{\partial^2 f_0^{(n)}}{\partial X_i \partial X_j} + \Omega_2^2 f_0^{(n)} = 0, \tag{19}$$

where there is no sum over the index $n$. The components of the tensor $T_{ij}^{nn}$ are formed from integrals over the cell involving the leading and first order solutions, and are given in Appendix B. This equation governs the propagation of long-wavelength

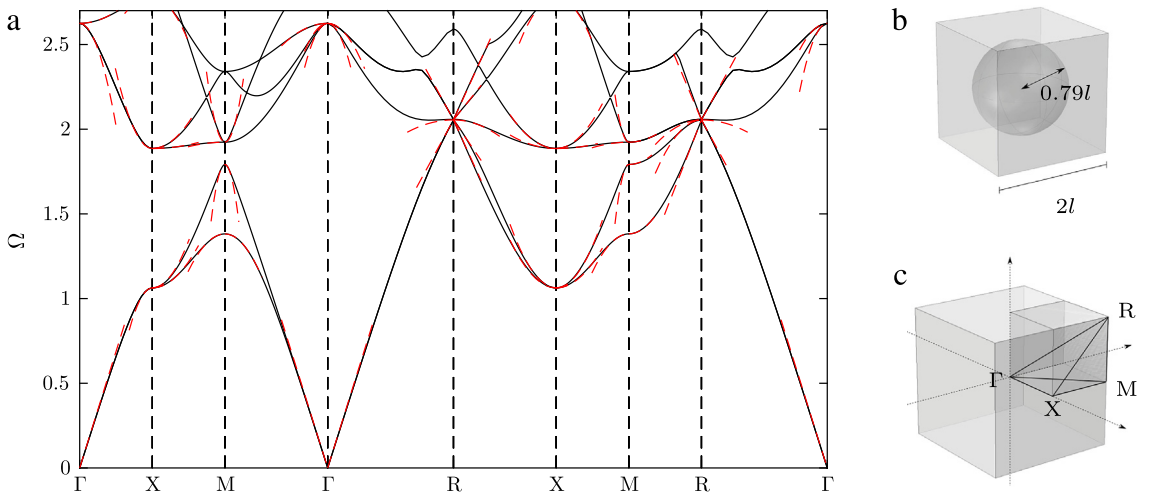


**Fig. 3.** (a) Photonic band diagram for a cubic array of perfectly-conducting spheres of radius $r = 0.79l$ in a background of air, as shown in (b). The band structure is plotted around the edges of the tetrahedral irreducible Brillouin zone (c). Solid black curves are from FEM calculation, and red dashed curves are asymptotics from Eqs. (15) and (19). Note the Dirac-like point at R, which occurs only at this particular value of the radius. (For interpretation of the references to colour in this figure legend, the reader is referred to the web version of this article.)

envelope functions inside the periodic structure, and the tensors $T_{ij}^{nn}$ contain information about the dynamic anisotropy associated with the modes.

As a means of verifying Eq. (19), we substitute in Bloch wave solutions of the form $f_0 = \exp(i\boldsymbol{\kappa} \cdot \mathbf{X}/\eta) = \exp(i\boldsymbol{\kappa} \cdot \mathbf{x}/l)$, where the dimensionless quantity $\boldsymbol{\kappa} = (\mathbf{k} - \mathbf{k_0})l$ is proportional to the difference between the Bloch vector at frequency $\Omega$ and that at $\Omega_0$, corresponding to the vertex of the irreducible Brillouin zone. This leads to locally quadratic behaviour of the dispersion bands as

$$\Omega = \Omega_0 + T_{ij}^{nn} \frac{\kappa_i \kappa_j}{2\Omega_0}. \tag{20}$$

In Fig. 3 we show the photonic band diagram for a cubic array of perfectly-conducting spherical inclusions, demonstrating that the asymptotics (red dashed curves) accurately capture the curvature of the bands in the vicinity of the Brillouin zone vertices. Note that the linear behaviour at R is due to an accidental degeneracy, induced by choosing the inclusion radius such that two eigenvalues coincide. In contrast, the other degeneracies observed in the band diagram are robust under the change of radius or material parameters, and can only be removed by breaking the symmetry of the cell; these are essential degeneracies.

### 3.2. Accidental degeneracies: linear dispersion

In the case of an accidental degeneracy, the object $P_j^{nr}$ generally contains non-zero elements, and the dispersion is governed to leading order by (15). Substituting in the Bloch wave solution $f_0^{(r)}(\mathbf{X}) = \hat{f}_0^{(r)} \exp(i\boldsymbol{\kappa} \cdot \mathbf{X}/\eta)$ for fixed small $\boldsymbol{\kappa}$ leads to a homogeneous matrix equation that can be solved numerically to give the linear asymptotic form of the dispersion relation.

It has been observed that under certain circumstances unusual wave guiding effects, as well as perfect transmission and cloaking, can be observed at Dirac-like points. Such behaviour is considered in detail in [36], where it is demonstrated that in some cases the linear dispersion can be mapped to that of a zero refractive index material. This is shown to occur if one can induce an accidental degeneracy between two triply degenerate eigenvalues at $\Gamma$ point, which is possible in a core–shell structure containing perfectly conducting inclusions. The local dispersion in this case is characterised by the crossing of two pairs of linear bands, with relatively flat quadratic bands passing through the middle, as seen in Fig. 4.

In order to extract an effective medium equation in the case of a Dirac-like point, we differentiate (15) once with respect to $X_i$, and then by self-substitution obtain

$$D_{ij}^{nr} \frac{\partial^2 f_0^{(r)}}{\partial X_i \partial X_j} + \Omega_1^4 f_0^{(n)} = 0, \tag{21}$$

where $D_{ij}^{nr} = -C_j^{np} C_i^{pr}$ and $C_j^{nr} = (Q^{-1})^{np} P_j^{pr}$. In general this system is intrinsically coupled and it is not possible to obtain separate equations governing the evolution of distinct modes. However, in the case of a point with isotropic dispersion, (21)

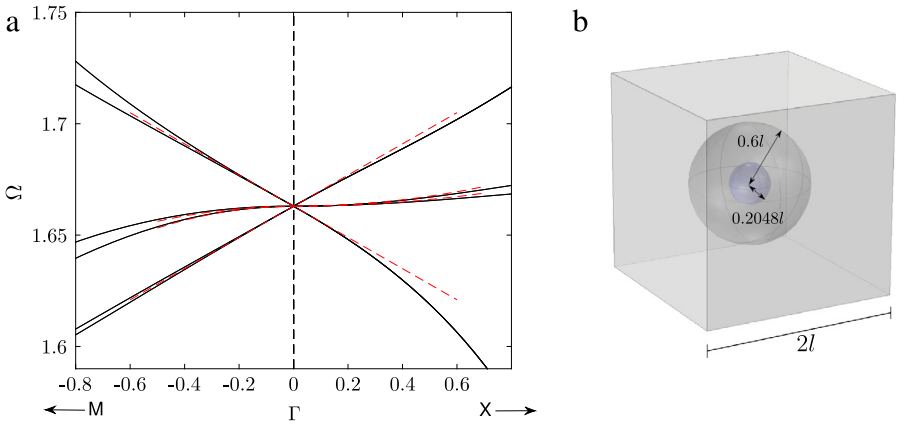


**Fig. 4.** (a) Dirac-like dispersion in a core–shell structure as demonstrated in [36]. Here the air-filled elementary cell (b) contains a spherical shell of permittivity 12 surrounding a perfectly conducting core. The effective equation governing the (repeated) linear branches is given by (22). The black solid curves are from full FEM calculation, and the red dashed lines are from the asymptotic dispersion relation. (For interpretation of the references to colour in this figure legend, the reader is referred to the web version of this article.)

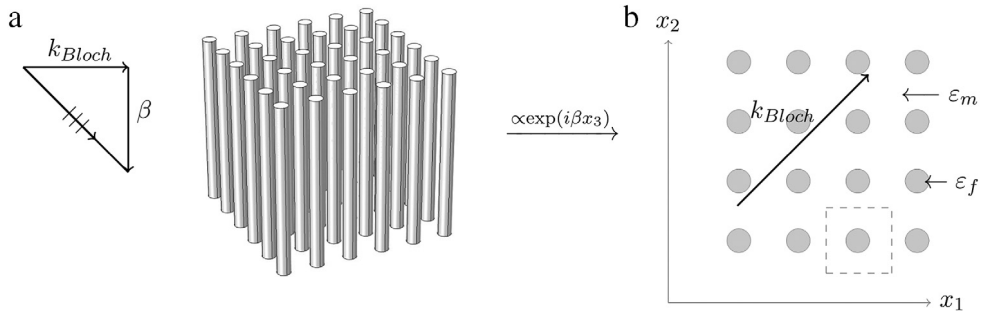


**Fig. 5.** Reduction of a typical fibre-like structure to two dimensions. As shown in (a), dielectric cylinders of permittivity $\varepsilon_c$ are embedded in a homogeneous matrix phase with permittivity $\varepsilon_m$. The resulting problem is projected onto the $(x_1, x_2)$ plane, and the angle of propagation depends on the ratio of the parameter $\beta$ and the planar Bloch wave vector, which characterises the phase shift across an irreducible cell (the dashed square in (b)).

naturally decouples to identical Helmholtz equations. In the example given above, we find four identical isotropic equations given by

$$0.054\nabla_X^2 f_0^{(n)} + \Omega_1^4 f_0^{(n)} = 0 \tag{22}$$

governing the linear bands, with a final pair exhibiting quadratic dispersion governed by (19). Eq. (22) may be written in terms of an effective refractive index $n_{\text{eff}} = c/v_g$, where $c$ is the speed of light in vacuum and $v_g$ is the speed of light:

$$\nabla^2 f_0 + n_{\text{eff}}^2 \varepsilon_0 \mu_0 \omega^2 f_0 = 0, \tag{23}$$

with $n_{\text{eff}}^2 = \varepsilon_0\mu_0(\omega^2 - \omega_0^2)^2 l^2/0.054\omega^2 \to 0$ as $\omega \to \omega_0$, and the leading-order magnetic field satisfies the same equation due to (11). This agrees with the result obtained in the article [36] using a scattering matrix method [37].

## 4. Application to PCFs

We now turn our attention to the case of dielectric cylinders of infinite length with constant permittivity $\varepsilon_f$ aligned in the $x_3$-direction and embedded in a matrix phase of permittivity $\varepsilon_m$. This model is appropriate for both holey-type PCFs, in which the cylinders are air holes in a dielectric background, as well as ARROW-type PCFs [38], in which the cylinders have a higher refractive index than the background. The $x_3$-dependence of the fields can be factored out as $\propto \exp(i\beta x_3)$ where $\beta$ is the propagation constant of the radiation, and the problem is reduced to a quasi-planar one. For a fixed value of $\beta$, the resulting Bloch wave structure is projected onto the $(x_1, x_2)$ plane, and the PDEs (15) and (19) govern propagation in these directions. Tuning $\beta$, along with the geometric and material properties of the cell, can then be used to induce particular features, such as partial stop-bands or Dirac-like points in the transverse plane. In Fig. 6, we show the band diagrams for one such configuration of air holes in a dielectric background at two different values of $\beta$, chosen such that a transverse stop-band and a Dirac-like point are exhibited. In order to obtain the quasi-planar analogues of (15) and (19), we simply make the substitutions $\partial/\partial X_3 \to 0$ and $\partial/\partial\xi_3 \to i\beta$ throughout the asymptotic hierarchy, and the corresponding integrals

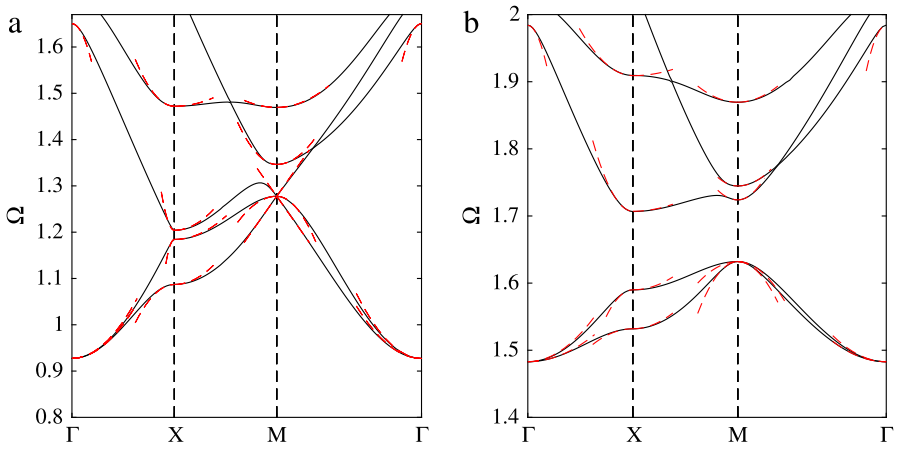


**Fig. 6.** Transverse photonic band diagrams for the lowest 5 bands for a square array of cylindrical air holes of radius $r = 0.75l$, where $2l$ is the pitch of the array, in a dielectric background with relative permittivity $\varepsilon_r = 6$. In (a), the parameter $\beta = 1.74/l$ has been tuned to induce an accidental degeneracy, resulting in a Dirac-like point at M. In (b), $\beta$ has been increased to $3/l$, causing the higher-frequency bands to separate from the lowest two, so the PCF exhibits a partial band gap in the transverse plane. Note that different scales have been used on the vertical axes. In both frames, the solid lines are from FEM calculation, and the dashed lines are the asymptotic approximations resulting from the planar analogues of (15) and (19).

become surface integrals over the two-dimensional cell. It is also straightforward to check for $\beta = 0$, in which case the solutions can be separated into TE and TM polarisations, that our theory reduces to that of scalar HFH, as published in [23].

### 4.1. Transverse stop bands and guided modes

The equations garnered from our asymptotic method govern the propagation of modes in photonic pass bands. The corresponding modes in the quasi-planar case propagate in the transverse plane as well as in the axial direction. Alternatively, we may consider a structure exhibiting a transverse stop band at a particular value of $\beta$, as shown in Fig. 6(b). If we introduce a finite defect of some kind into the structure, it may be possible to excite a mode whose frequency lies within the stop band, and hence decays evanescently in the surrounding structure. If the frequency lies in the vicinity of one of the eigenfrequencies $\Omega_0$, the decay is then predominantly governed by (19). In Fig. 7(a), we show one such mode, calculated using the eigenvalue solver within the Wave Optics module of Comsol Multiphysics® 5.0 [39], where one air cylinder is removed from a large but finite array of cells corresponding to Fig. 6(b), with perfect electrical conducting (PEC) conditions on the surrounding boundary. The guided mode is at $\Omega = 1.690$, close to the standing wave frequency $\Omega_0 = 1.707$, corresponding to the third eigenvalue at X in Fig. 6(b). We observe highly-directed leakage, which is explained by the dominant long-scale equation, in this case given by

$$1.01\frac{\partial^2 f_0}{\partial X_1^2} + 0.098\frac{\partial^2 f_0}{\partial X_2^2} + \Omega_2^2 f_0 = 0. \tag{24}$$

The fact that the first term has a coefficient of far greater magnitude than the second leads to directed decay in the $x_1$-direction, and hence also in the $x_2$-direction due to the symmetry point X′, the reflection of the point X in the line $x_1 = x_2$. The decay of the envelope surrounding the mode in these directions is then very well approximated by an exponential form $\exp(-\alpha x)$, where the decay rate $\alpha = 0.24/l$ follows from (24). Frame (b) shows the absolute value of the field along the axis labelled $x$ in (a), and the red dashed envelope shows the exponentially-decaying envelope $\exp(-\alpha x)$.

## 5. Application to array-guided surface waves

For various wave systems, it is well known that periodic structures embedded in otherwise homogeneous media can support localised modes. Such modes exhibit Bloch wave quasi-periodicity in the array, and decay evanescently in the surrounding medium, reminiscent of Rayleigh waves at the surface of solids. It is therefore natural to describe them as Rayleigh–Bloch modes, and their existence is ubiquitous in systems where the dimensionality of the array is at least one less than that of the wave system in question. Rayleigh–Bloch waves are distinguished from ‘pure’ surface waves (e.g. Rayleigh waves, Lamb waves, etc.) in that they can propagate along surfaces that exhibit some material or geometric periodicity and which, in the absence of this periodicity, do not support surface waves. In this sense they are similar to spoof surface plasmons [40]. In two- and three-dimensional systems, linear arrays may be employed as diffraction gratings, and have been studied in the context of water waves and acoustics as solutions to the Helmholtz equation [41,42,32], surface plasmons [43,44], as well as coupled elastic waves [26]. In three-dimensional systems, such as the vector Maxwell system, Rayleigh–Bloch modes can exist for linear or planar arrays [33], the latter allowing for the possibility of a range of in-plane

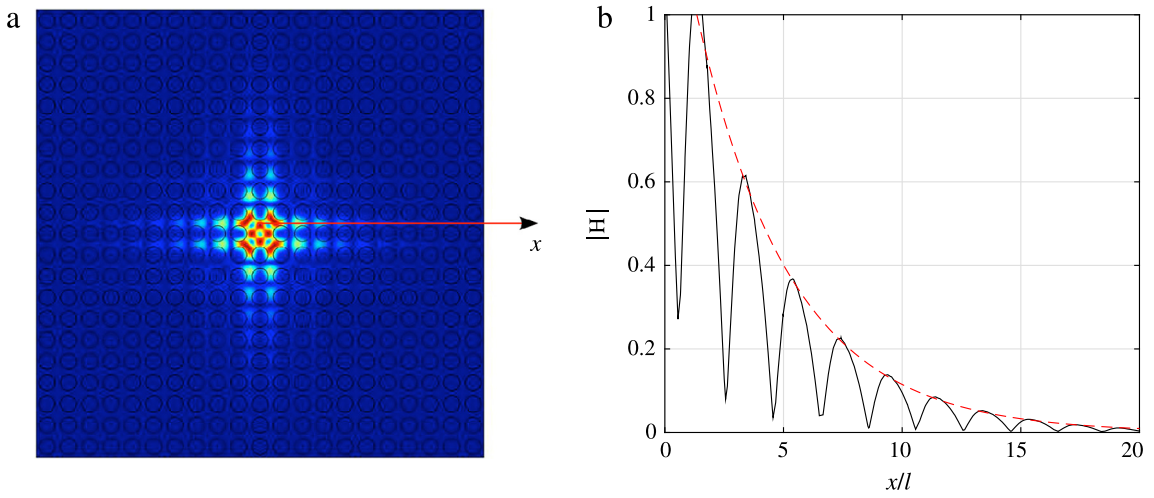


**Fig. 7.** (a) Magnetic field norm for a localised defect mode at $\Omega = 1.690$, induced by removing one air cylinder from a large array of cells (of which a portion are shown here), corresponding to those of Fig. 6(b). Frame (b) shows the absolute value of the field along the axis labelled $x$ in (a), and the red dashed envelope shows the exponentially-decaying envelope $\exp(-\alpha x)$. (For interpretation of the references to colour in this figure legend, the reader is referred to the web version of this article.)

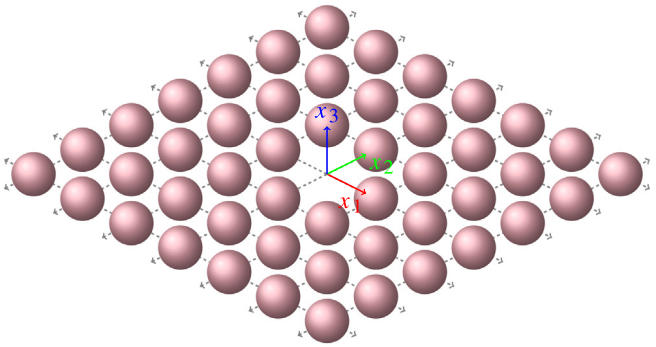


**Fig. 8.** A Doubly-periodic planar square array of dielectric spheres. For the purpose of computation, the spheres have radii of $0.8l$, where the pitch of the array is $2l$. The spheres are embedded in free space and have a relativity permittivity $\varepsilon_r = 20$. Note the sphere at the origin is omitted from the figure to allow the axes labels to be visible, and not absent in the computations.

effects to be observed. Rayleigh–Bloch waves are also referred to as array-guided surface waves, bound states, and Bloch surface waves, depending on the context.

The asymptotic technique we have developed is particularly well-suited to studying electromagnetic Rayleigh–Bloch systems, as the corresponding full numerical computations can be prohibitively demanding, particularly for fully coupled three-dimensional problems of the type examined here. In order to assess and demonstrate the efficacy of the asymptotic technique developed in the preceding sections, we consider an infinite doubly-periodic planar array of dielectric spheres embedded in free space, as depicted in Fig. 8. Once again, the theory is largely unaltered from the three-dimensional case; we simply make the substitution $\partial/\partial X_3 \to 0$ in (15) and (19), and extend the cell in the $\xi_3$-direction as shown in Fig. 9(b). Since we are only concerned with surface modes, that is, modes which decay exponentially in the $\pm\xi_3$ direction, the elementary cell is extended vertically such that all fields decay sufficiently before reaching the boundary; we apply PEC conditions on these boundaries for computational efficiency, as opposed to PML, since PML creates a continuum of spurious modes.

The corresponding photonic band diagram is shown in Fig. 9(a) where we plot only those modes that exist below the light-cone, indicated by the thick black lines in Fig. 9(a). These modes are those of primary interest and correspond to modes localised to the grating, i.e. they do not radiate energy to $\xi_3 = \pm\infty$. Modes corresponding to dispersion curves above the light-cones are associated with waves with propagative components in the $\xi_3$ direction.

### 5.1. Planar dynamic anisotropy and hyperbolic surface modes on gratings

The band diagram of Fig. 9 has several interesting features including a planar band-gap as well as nearly flat bands associated with so-called *slow waves*. A particularly fascinating feature is the change in curvature of the lowest branch at lattice point X in the reciprocal space, shown in the inset of Fig. 9(a) along with the corresponding local asymptotics. Such

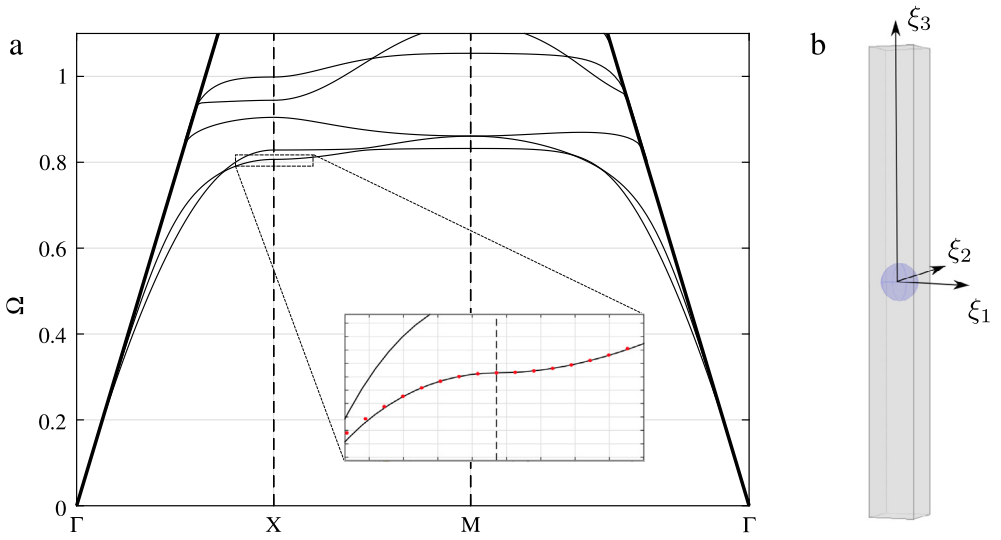


**Fig. 9.** (a) In-plane photonic band diagram for a square array of high-permittivity ($\varepsilon_r = 20$) dielectric spheres in vacuum, as shown in Fig. 8. The radius of the spheres is $0.8l$, where $2l$ is the pitch of the array, corresponding to the elementary cell (b). Here the cell is extended in the $\xi_3$-direction, and perfectly conducting boundary conditions are applied at its top and bottom of the cell. The inset of (a) shows an enlarged portion of the diagram in which the local behaviour is governed by the hyperbolic effective equation $-0.19f_{0,x_1x_1} + 0.11f_{0,x_2x_2} + \Omega_2^2 f_0 = 0$, leading to the asymptotics shown by red dots. (For interpretation of the references to colour in this figure legend, the reader is referred to the web version of this article.)

saddle points are associated with dynamic anisotropy [45–47] and hyperbolic materials [48,49]; this type of media, when excited by an appropriate multipole source, direct the electromagnetic energy along clearly defined characteristic lines. The existence of these saddle points for the system under consideration suggests the interesting possibility of dynamic anisotropy in a Rayleigh–Bloch wave setting, creating an effective hyperbolic surface.

We used the asymptotic theory developed earlier to obtain the leading order solution for the field when the array is excited by a dipole source at a frequency close to that of the saddle point on the dispersion surface ($\Omega_0 = 0.8071$). This involves solving the leading and first order cell problems as outlined in Section 3, and the solvability condition for the second-order problem then generates a PDE, of the same form as (19), for the long-scale function $f_0$:

$$T_{ij}\frac{\partial^2 f_0}{\partial x_i \partial x_j} + \frac{(\omega^2 - \omega_0^2)}{c^2} f_0 = 0, \tag{25}$$

where $T$ is now a rank-2 tensor. In this case, we find that $T = \mathrm{diag}(-0.19, 0.11)$ is diagonal and $T_{11}T_{22} < 0$, yielding a hyperbolic PDE on the long-scale. The leading order asymptotic field for the forced problem is then a superposition of the solution to this PDE, whose forcing must take into account the symmetry of the cell problem, along with its symmetrical counterpart excited at point X′, the reflection of the point X in the line $x_1 = x_2$. The result is most striking when the electric field is plotted, as we do here, and since the hyperbolic mode is primarily out-of-plane electric, we only include the $E_3$-component of the field. Both the cell and long-scale problems were solved using the commercial finite element package Comsol Multiphysics® 5.0.

For comparison the above problem is also treated, purely numerically, using finite elements. In particular, a $37 \times 37$ planar array of spheres is considered; the finite cluster is surrounded by regions of perfectly matched layers in order to simulate an infinite domain. Moreover, the computational cost of the full finite element simulation is lessened by making full use of the available symmetries, thereby reducing the computational domain by a factor of 8. The array is then excited at its centre by a dipole source of unitary magnitude and oriented along the $x_3$-axis. The material and geometrical parameters of the array correspond to the dispersion diagram presented in Fig. 9 and are detailed in the figure caption. The $E_3$-component of the electric field from the full numerical simulation is shown in Fig. 10(b) and should be compared with the asymptotic field shown in Fig. 10(a). For comparison, we also plot the field along the line $(x, y, z) = (x, x, 0)$ and passing through the dipole source (see Fig. 10(c)).

The novel exhibition of dynamic anisotropy on a grating, and the creation of an effective hyperbolic surface, is an exciting effect with several potential applications in the guiding of surface waves; this effect allows not only the confinement of waves to a surface or interface, but also the control of their propagation upon the surface itself. These effects occur, by necessity, at frequencies where the wavelength is comparable to the size of the microstructure where traditional (long-wave) homogenisation theories are no longer valid. However, as demonstrated by Fig. 10, the asymptotic homogenisation scheme developed here is capable of accurately and conveniently describing such effects.

Although we have not carried out a comprehensive analysis of the computational cost of the asymptotic method, it is illuminating to consider the following: The full finite element simulation, using all the available symmetries, required

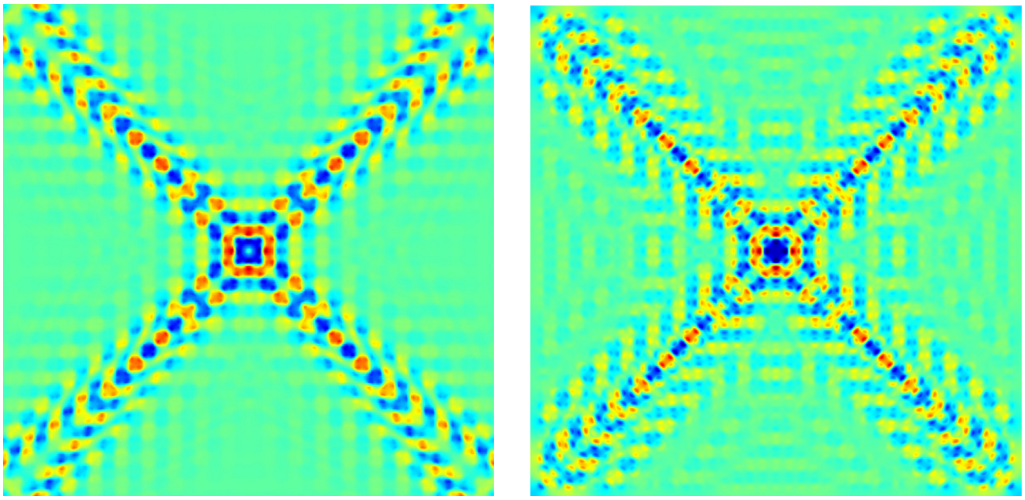

(a) Asymptotic analysis. (b) Finite element simulation.

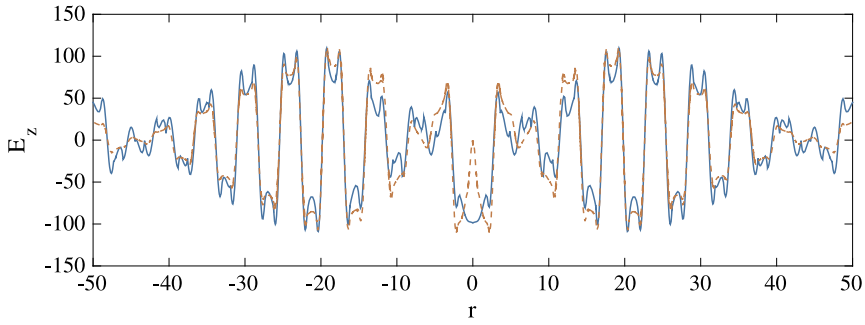


(c).

**Fig. 10.** The $z$-component of the real part of the electric field for the planar array obtained from (a) the asymptotic analysis and (b) the full finite element simulations. In both cases the colour scale is linear running for minimum (blue), through zero (green) to maximal (red). Part (c) shows the $z$-component of the real part of the electric field plotted along a line passing through the points $\boldsymbol{x} = (0, 0, 0)$ and $(1, 1, 0)$. The solid curve represents the field from the full finite element simulation, whereas the dashed curve corresponds to the leading order solution from the asymptotic analysis. The non-dimensional angular frequency of excitation is $\Omega = 0.80705$, which is close to the resonant frequency of $\Omega_0 = 0.8071$. (For interpretation of the references to colour in this figure legend, the reader is referred to the web version of this article.)

approximately 16.8 million degrees of freedom and took 11.5 h to solve on a dedicated machine using 77 GB of RAM and 16 processor cores running at 2.5 GHz. In comparison, the numerical element of the asymptotic scheme used around 830 thousand degrees of freedom, 3.7 GB of RAM and required 2.7 min to solve on a laptop with 2 cores running at 2.8 GHz.

## 6. Concluding remarks

We have demonstrated that in the vicinity of Brillouin zone vertices for a periodic structure, photonic modes governed by the vector Maxwell system satisfy second-order scalar PDEs, whose solutions govern the propagation, or decay, of waves in the bulk of the structure. In some cases, these PDEs can be used straightforwardly to predict qualitatively and quantitatively the long-scale behaviour of the photonic structure, which has been demonstrated in the context of a forced problem in a planar PC, as well as an eigenvalue problem for a guided mode in a PCF.

In the case of the PCF, we showed that the asymptotic methodology correctly predicted the decay rate of an envelope function surrounding the electromagnetic field around a core defect in an array of cylinders at a band-gap frequency. An intriguing possibility would be to extend this work to pose an effective eigenvalue problem for guided modes in a PCF. This would involve connecting a local eigenvalue problem for the core defect to a decaying field away from the core, which may be described asymptotically and to leading order by equations of the form derived in this paper. This is an challenging problem that would be approached using the method of matched asymptotic expansions.

A particularly interesting physical example was considered in Section 5 wherein the asymptotic theory was applied to a fully coupled three-dimensional problem for the Maxwell system. Using a planar array of dielectric spheres we were able to create an effective hyperbolic interface which supports surface waves that also exhibit dynamic anisotropy over the surface.

One can envisage many applications where the ability to guide electromagnetic waves along a surface whilst also controlling the propagation over the surface itself would be useful.

A natural extension of this work is to consider more general Bravais geometries that are not necessarily square/cubic. In fact, such work has recently been completed for the simpler case of TE-polarised radiation [50], and it is clear that much of the theory presented here carries through unaltered. A second extension would be to consider structures with a wider range of material properties, for example those experiencing dielectric loss, or perhaps more interestingly realistic models of metals, whose frequency-dependent properties can be described by the Drude model.

**Acknowledgements**

The authors thank the EPSRC for support through research grants (EP/I018948/1, EP/L024926/1, EP/J009636/1) and Mathematics Platform grant (EP/I019111/1).

## Appendix A. The $O(\eta)$ compatibility condition

In this appendix we derive Eq. (15) as a compatibility condition for the $\mathcal{O}(\eta)$ system. For each $n \in \{1, 2, \ldots, p\}$, we take the scalar product of (13) with $\mathbf{h}_0^{(n)*}$ and subtract from the scalar product of (9)* with $\mathbf{H}_1/f_0^{(n)}$. The resulting equation reads

$$\begin{aligned}&\mathbf{h}_0^{(n)*}\cdot\nabla_\xi\times\varepsilon_{\mathrm{r}}^{-1}\nabla_\xi\times\mathbf{H}_1-\mathbf{H}_1\cdot\nabla_\xi\times\varepsilon_{\mathrm{r}}^{-1}\nabla_\xi\times\mathbf{h}_0^{(n)*}\\&\quad=\mathbf{h}_0^{(n)*}\cdot\left(-\nabla_\xi\times\varepsilon^{-1}\nabla_X\times\mathbf{H}_0-\varepsilon_{\mathrm{r}}^{-1}\nabla_X\times\nabla_\xi\times\mathbf{H}_0+\mu_{\mathrm{r}}\Omega_1^2\mathbf{H}_0\right).\end{aligned}\tag{26}$$

Using the vector identity $\mathbf{A}\cdot(\nabla\times\nabla\times\mathbf{B})-\mathbf{B}\cdot(\nabla\times\nabla\times\mathbf{A})=\nabla\cdot\left(\mathbf{B}\times\nabla\times\mathbf{A}-\mathbf{A}\times\nabla\times\mathbf{B}\right)$ [51], the left hand side of this is

$$\varepsilon_{\mathrm{r}}^{-1}\nabla_\xi\cdot\left(\mathbf{H}_1\times\nabla_\xi\times\mathbf{h}_0^{(n)*}-\mathbf{h}_0^{(n)*}\times\nabla_\xi\times\mathbf{H}_1\right)+(\nabla_\xi\varepsilon_{\mathrm{r}}^{-1})\cdot\left(\mathbf{H}_1\times\nabla_\xi\times\mathbf{h}_0^{(n)*}-\mathbf{h}_0^{(n)*}\times\nabla_\xi\times\mathbf{H}_1\right),\tag{27}$$

which is simply the divergence of the quantity $\varepsilon_{\mathrm{r}}^{-1}\left(\mathbf{H}_1\times\nabla_\xi\times\mathbf{h}_0^{(n)*}-\mathbf{h}_0^{(n)*}\times\nabla_\xi\times\mathbf{H}_1\right)$. Integrating this over the elementary cell $\mathcal{C}$ and applying the divergence theorem leaves us with an integral over the surface of the cell which vanishes by periodicity/antiperiodicity of $\mathbf{H}_1$ and $\mathbf{h}_0^{(n)}$, along with a non-vanishing contribution at the phase boundaries given by

$$\int_{\cup\partial\mathcal{D}_{1,2}}\left[\varepsilon_{\mathrm{r}}^{-1}\left\{\mathbf{h}_0^{(n)*}\cdot\left(\mathbf{n}\times\nabla_\xi\times\mathbf{H}_1\right)-\mathbf{H}_1\cdot\left(\mathbf{n}\times\nabla_\xi\times\mathbf{h}_0^{(n)*}\right)\right\}\right]\mathrm{d}S,\tag{28}$$

where again square brackets denote a jump discontinuity. The continuity conditions on $\mathbf{H}_1$ and $\mathbf{e}_0^{(n)}$ ensure that the only non-zero contribution comes from the first term above, and we are left with the following equation:

$$\int_{\cup\partial\mathcal{D}_{1,2}}\left[\varepsilon_{\mathrm{r}}^{-1}\mathbf{h}_0^{(n)*}\cdot\left(\mathbf{n}\times\nabla_\xi\times\mathbf{H}_1\right)\right]\mathrm{d}S=\int_{\mathcal{C}}\mathbf{h}_0^{(n)*}\cdot\left\{-\nabla_\xi\times\varepsilon_{\mathrm{r}}^{-1}\nabla_X\times\mathbf{H}_0-\varepsilon_{\mathrm{r}}^{-1}\nabla_X\times\nabla_\xi\times\mathbf{H}_0+\mu_{\mathrm{r}}\Omega_1^2\mathbf{H}_0\right\}\mathrm{d}V,\tag{29}$$

for $n = 1, 2, \ldots, p$. Using the cyclic property of the scalar triple product, the first term of the integrand on the right is $\nabla_\xi\cdot\left(\mathbf{h}_0^{(n)*}\times\varepsilon_{\mathrm{r}}^{-1}\nabla_X\times\mathbf{H}_0\right)-\varepsilon_{\mathrm{r}}^{-1}\left(\nabla_\xi\times\mathbf{h}_0^{(n)*}\right)\cdot\left(\nabla_X\times\mathbf{H}_0\right)$. Applying the divergence theorem to the first resulting term yields a surface integral which, with the help of the continuity conditions, exactly cancels the surface integral on the left hand side of (29), leaving the equation

$$0=\int_{\mathcal{C}}\left\{-\varepsilon_{\mathrm{r}}^{-1}\left(\nabla_\xi\times\mathbf{h}_0^{(n)*}\right)\cdot\left(\nabla_X\times\mathbf{H}_0\right)-\varepsilon_{\mathrm{r}}^{-1}\mathbf{h}_0^{(n)*}\cdot\nabla_X\times\nabla_\xi\times\mathbf{H}_0+\mu_{\mathrm{r}}\Omega_1^2\mathbf{h}_0^{(n)*}\cdot\mathbf{H}_0\right\}\mathrm{d}V.\tag{30}$$

Now, substituting the leading-order solution $\mathbf{H}_0=f_0^{(r)}\mathbf{h}_0^{(r)}$, noting that $\varepsilon_{\mathrm{r}}^{-1}\nabla_\xi\times\mathbf{h}_0^{(n)}=-i\Omega_0\mathbf{e}_0^{(n)}$, leads to the system of Eqs. (15).

## Appendix B. The $O(\eta^2)$ compatibility condition

In this appendix we derive (19) as a compatibility condition for the $\mathcal{O}(\eta^2)$ system, following a similar methodology to that of Appendix A; we begin by taking the scalar product of (17) with $\mathbf{h}_0^{(n)*}$, subtract from the scalar product of (9)* with $\mathbf{H}_2/f_0^{(n)}$, and integrate the resulting equation over the elementary cell $\mathcal{C}$. The left hand side vanishes like the first order equivalent, leaving

$$\begin{aligned}&\int_{\mathcal{C}}\left\{-\varepsilon_{\mathrm{r}}^{-1}\left(\nabla_\xi\times\mathbf{h}_0^{(n)*}\right)\cdot\left(\nabla_X\times\mathbf{H}_1\right)-\varepsilon_{\mathrm{r}}^{-1}\mathbf{h}_0^{(n)*}\cdot\nabla_X\times\nabla_\xi\times\mathbf{H}_1\right.\\&\left.\quad-\varepsilon_{\mathrm{r}}^{-1}\mathbf{h}_0^{(n)*}\cdot\nabla_X\times\nabla_X\times\mathbf{H}_0+\mu_{\mathrm{r}}\Omega_2^2\mathbf{h}_0^{(n)*}\cdot\mathbf{H}_0\right\}\mathrm{d}V=0.\end{aligned}\tag{31}$$

Using the cyclic property of the scalar triple product, it is straightforward to show that the contribution of the complementary part of $\mathbf{H}_1$ in the above equation is zero. Changing to tensor notation, and making use of the contracted epsilon identity $\epsilon_{ijk}\epsilon_{klm} = \delta_{il}\delta_{jm} - \delta_{im}\delta_{jl}$, we are led to the following system of effective PDEs:

$$\hat{T}_{ij}^{nr}\frac{\partial^2 f_0^{(r)}}{\partial X_i \partial X_j} + \Omega_2^2 Q^{nr} f_0^{(r)} = 0 \Longleftrightarrow T_{ij}^{nr}\frac{\partial^2 f_0^{(r)}}{\partial X_i \partial X_j} + \Omega_2^2 f_0^{(n)} = 0, \tag{32}$$

where $T_{ij}^{nr} = (Q^{-1})^{nq}\hat{T}_{ij}^{qr}$, with $Q^{nr} = \int_{\mathcal{C}} \mu_r h_{0k}^{(n)*} h_{0k}^{(r)} \mathrm{d}V$ and

$$\hat{T}_{ij}^{nr} = \int_{\mathcal{C}} \varepsilon_r^{-1}\left\{\delta_{ij}h_{0k}^{(n)*}h_{0k}^{(r)} - h_{0j}^{(n)*}h_{0i}^{(r)} + h_{1kj}^{(r)}\partial_k h_{0i}^{(n)*} - h_{1kj}^{(r)}\partial_i h_{0k}^{(n)*} + h_{0k}^{(n)*}\partial_i h_{1kj}^{(r)} - h_{0k}^{(n)*}\partial_k h_{1ij}^{(r)}\right\}\mathrm{d}V. \tag{33}$$

In the case of a distinct eigenvalue, the above system reduces to a single equation with $n = r = 1$. For a repeated eigenvalue, the substitution $f_0^{(r)}(\mathbf{X}) = \hat{f}_0^{(r)}\exp(i\kappa\cdot\mathbf{X}/\eta)$ yields a homogeneous matrix equation whose solution gives the quadratic asymptotics, but in fact the independent Bloch modes are non-interacting in the sense that they can be decoupled as:

$$M^{np}\tilde{T}_{ij}^{pq}(M^{-1})^{qr}\frac{\partial^2 f_0^{(r)}}{\partial X_i \partial X_j} + \Omega_2^2 f_0^{(n)} = 0, \tag{34}$$

where $M$ is matrix of eigenvectors shared by the matrices $T_{ij}$, and hence $\tilde{T}_{ij}$ are all diagonal matrices. Pre-multiplying by $M^{-1}$, we are then left with the decoupled system

$$\tilde{T}_{ij}^{nr}\frac{\partial^2 \tilde{f}_0^{(r)}}{\partial X_i \partial X_j} + \Omega_2^2 \tilde{f}_0^{(n)} = 0, \tag{35}$$

where $\tilde{f}_0^{(n)} = (M^{-1})^{nr} f_0^{(r)}$. We can write the general leading order solution as a linear combination of these decoupled modes $\mathbf{H}_0 = \tilde{f}_0^{(r)}\tilde{\mathbf{h}}_{\mathbf{0}}^{(r)}$, with $\tilde{\mathbf{h}}_{\mathbf{0}}^{(n)} = M^{rn}\mathbf{h}_0^{(r)}$. Note that the tildes have been omitted in Eq. (19) as it is assumed that the decoupling is done automatically.

## Appendix C. Low-frequency quasi-static limit

In this appendix we show that for a dielectric structure (for which $\mu \equiv 1$) at low frequencies, the system of Eqs. (32) can be written in the familiar vector form of classical homogenisation theory, given by

$$-\nabla\times(\varepsilon^{-1,\mathrm{hom}}\nabla\times\mathbf{H}_0) + \omega^2\mu_0\mathbf{H}_0 = 0, \tag{36}$$

where $\varepsilon_{ij}^{-1,\mathrm{hom}} = \langle\varepsilon^{-1}\rangle\delta_{ij} + \tilde{\varepsilon}_{ij}^{-1}$. Here $\langle\cdot\rangle$ denotes a cell-averaged quantity, and the correction tensor $\tilde{\varepsilon}_{ij}^{-1}$ has components depending on the specific geometry of the cell. This will be possible only in the quasi-static regime where the frequency is sufficiently low that the field on the cell level is characterised by a small perturbation to an otherwise constant field. Formally, this occurs when $\Omega^2 = \mathcal{O}(\eta^2)$, corresponding to the substitution $\Omega_0 = 0$ into the leading order system.

Following the HFH procedure of Section 3, we deduce that the leading order eigensolution is a constant vector field, and $\Omega_0 = 0$ is thus to be treated as a repeated eigenvalue with multiplicity $p = 3$, corresponding to the three spatial directions. The eigensolutions can be chosen without loss of generality to be oriented along each of the three ordinate axes so that $h_{0i}^{(n)} = \delta_{ni}$, and hence $\mathbf{H}_0 = (f_0^{(1)}, f_0^{(2)}, f_0^{(3)})^T$.

We need to access the algebra of Appendix B and compare Eq. (36) to the HFH result for repeated eigenvalues, (32); the two are identical if we can write $T_{ij}^{nr} = \epsilon_{nik}\epsilon_{jrl}\varepsilon_{kl}^{-1,\mathrm{hom}}$ for some second-rank tensor $\varepsilon_{kl}^{-1,\mathrm{hom}}$, which is equivalent to the statement that the tensor $T$ contains the following symmetries: $T_{ij}^{nr} = T_{nr}^{ij} = -T_{ir}^{nj} = -T_{nj}^{ir}$. Substituting the constant fields into (32) we find the explicit form for $T$ as

$$T_{ij}^{nr} = \int_{\mathcal{C}} \varepsilon_r^{-1}\left(\delta_{ij}\delta_{nr} - \delta_{jn}\delta_{ir} + \partial_i h_{1nj}^{(r)} - \partial_n h_{1ij}^{(r)}\right)\mathrm{d}V. \tag{37}$$

It is straightforward to show that the first two terms in the integrand satisfy the necessary symmetries, which are inherited directly from the $-\nabla_X\times\nabla_X\times(\cdot)$ operator in (31). It is also trivial to note that the remaining two terms are antisymmetric in $n$ and $i$. The only non-trivial symmetry that remains is antisymmetry of the second two terms with respect to $j$ and $r$. In order to prove this, we consider the inhomogeneous problem (13): substituting in the constant leading order solutions, along with the candidate particular solution $H_{1i} = f_{0,X_j}^{(r)} h_{1ij}^{(r)}$ leads to the following coupled problems for $i, j, r \in \{1, 2, 3\}$:

$$\partial_k(\varepsilon_r^{-1}\partial_k h_{1ij}^{(r)}) - \partial_k(\varepsilon_r^{-1}\partial_i h_{1kj}^{(r)}) = \delta_{ij}\partial_r\varepsilon_r^{-1} - \delta_{ir}\partial_j\varepsilon_r^{-1}, \tag{38}$$

subject to boundary conditions at any phase interface given by

$$\left[\varepsilon_{\mathrm{r}}^{-1}\partial_k h_{1ij}^{(r)} n_k - \varepsilon_{\mathrm{r}}^{-1}\partial_i h_{1kj}^{(r)} n_k\right]_{\mathcal{D}_{1,2}} = \left[\varepsilon_{\mathrm{r}}^{-1}\right]_{\mathcal{D}_{1,2}} (\delta_{ij} n_r - \delta_{ir} n_j), \tag{39}$$

where $n_i$ is the component of the unit normal $\mathbf{n}$ in the $x_i$-direction and $[\cdot]$ denotes a jump discontinuity. The two-scale expansion of the divergence-free condition $\nabla_\xi \cdot \mathbf{H_1} = -\nabla_X \cdot \mathbf{H_0}$ must also be satisfied, which gives $f_{0,X_j}^{(r)} h_{1ij,\xi_i}^{(r)} = -f_{0,X_j}^{(r)} \delta_{jr}$. In the case that $j \neq r$, this condition is homogeneous, and because the right hand sides of both (38) and (39) are antisymmetric in $j$, $r$, we deduce that $h_{1ij}^{(r)} = -h_{1ir}^{(j)}$. On the other hand, for $j = r$ the divergence-free condition yields $h_{1ij,\xi_i}^{(r)} = -1$. Integrating this over the cell $\mathcal{C}$ and applying the divergence theorem and periodicity leads to a contradiction "$0 = 1$" that can only be avoided if $f_{0,X_j}^{(r)} \delta_{jr} = 0$. We have hence derived the long-scale divergence-free condition $\nabla_X \cdot \mathbf{H_0} = 0$, and with this in place we can show for $j = r$ that $h_{1,ij}^{(r)} = 0$. In doing so, $T$ is deduced to contain the correct symmetries, and we derive an expression for the effective permittivity as follows:

$$T_{ij}^{nr} = \epsilon_{nik}\epsilon_{jrl}\varepsilon_{kl}^{-1,\mathrm{hom}} \Longrightarrow \varepsilon_{kl}^{-1,\mathrm{hom}} = \frac{1}{(2!)^2}\epsilon_{nik}\epsilon_{jrl}T_{ij}^{nr}. \tag{40}$$

For each permutation of $k$, $l$, we only need evaluate one component of $T$. It is natural to split the resulting inverse permittivity tensor into a sum of two parts, the first resulting from the Kronecker delta terms in the integrand of $T_{ij}^{nr}$, given by $\langle\varepsilon^{-1}\rangle\delta_{ij}$, and the second from the two remaining terms, which we refer to as the correction tensor $\tilde{\varepsilon}_{ij}^{-1}$. Putting all this together we recover (36) and hence the quasi-static homogenisation of Maxwell's equations in dielectric media.

## References


[1] V.G. Veselago, The electrodynamics of substances with simultaneously negative values of $\epsilon$ and $\mu$, Sov. Phys. Usp. 10 (1968) 509–514.
[2] J.B. Pendry, Negative refraction makes a perfect lens, Phys. Rev. Lett. 85 (2000) 3966–3969.
[3] A. Alù, First-principles homogenization theory for periodic metamaterials, Phys. Rev. B 84 (2011) 075153.
[4] S. Guenneau, F. Zolla, Homogenization of three-dimensional finite photonic crystals, Prog. Electromagnetics Res. 27 (2000) 91–127.
[5] S. Guenneau, F. Zolla, A. Nicolet, Homogenization of three-dimensional photonic crystals with heterogeneous permittivity and permeability', Waves Random Complex Media 17 (4) (2007) 653–697.
[6] O. Ouchetto, S. Zouhdi, A. Bossavit, G. Griso, B. Miara, Modeling of 3-d periodic multiphase composites by homogenization, IEEE Trans. Microw. Theory Tech. 54 (6) (2006) 2615–2618.
[7] N. Wellander, G. Kritensson, Homogenisation of the Maxwell equations at fixed frequency, SIAM J. Appl. Math. 64 (1) (2003).
[8] M.Sh. Birman, T.A. Suslina, Second order periodic differential operators. Threshold properties and homogenization, St. Petersburg Math. J. 15 (2004) 639–714.
[9] Sihvola, Electromagnetic Mixing Formulae and Applications, The Institute of Electrical Engineers, London, 1999.
[10] C.L. Holloway, E.F. Kuester, J.A. Gordon, J. O'Hara, J. Booth, D.R. Smith, An overview of the theory and applications of metasurfaces: The two-dimensional equivalents of metamaterials, IEEE Antennas Propag. Mag. 54 (2012) 10–35.
[11] A.A. Maradudin (Ed.), Structured Surfaces as Optical Metamaterials, Cambridge University Press, 2011.
[12] E.F. Kuester, A.M. Mohamed, M. Piket-May, C.L. Holloway, Averaged transition conditions for electromagnetic fields at a metafilm, IEEE Trans. Antennas and Propagation 51 (10) (2003) 2641–2651.
[13] C.L. Holloway, E.F. Kuester, A. Dienstfrey, A homogenization technique for obtaining generalized sheet transition conditions for an arbitrarily shaped coated wire grating, Radio Sci. 49 (2014) 813–850.
[14] C.L. Holloway, E.F. Kuester, Corrections to the classical continuity conditions at the interface of a composite medium, Photonics Nanostruct. Fundam. Appl. 11 (4) (2013) 397–422.
[15] C.L. Holloway, E.F. Kuester, The homogenization-based derivation of effective boundary conditions for perfectly conducting periodic surfaces with a cover layer, Radio Sci. 35 (3) (2000) 661–681.
[16] C.L. Holloway, E.F. Kuester, Impedance-type boundary conditions for a periodic interface between a dielectric and a highly conducting medium, IEEE Trans. Antennas and Propagation 48 (10) (2000) 1660–1672.
[17] J.D. Joannopoulos, S.G. Johnson, J.N. Winn, R.D. Meade, Photonic Crystals, Molding the Flow of Light, second ed., Princeton University Press, Princeton, 2008.
[18] H. Benisty, Photonic crystals: New designs to confine light, Nat. Phys. 1 (1) (2005) 9–10. 10.
[19] D.N. Chigrin, S. Enoch, C.M. Sotomayer Torres, G. Tayeb, Self-guiding in two-dimensional photonic crystals, Opt. Express 11 (2003) 1203–1211.
[20] J.P. Dowling, C.M. Bowden, Anomalous index of refraction in photonic bandgap materials, J. Modern Opt. 41 (1994) 345–351.
[21] M. Notomi, Theory of light propagation in strongly modulated photonic crystals: Refractionlike behavior in the vicinity of the photonic band gap, Phys. Rev. B 62 (16) (2000) 10696–10705.
[22] S.G. Johnson, J.D. Joannopoulos, Block-iterative frequency-domain methods for Maxwell's equations in a planewave basis, Opt. Express 8 (2001) 173–190.
[23] R.V. Craster, J. Kaplunov, A.V. Pichugin, High-frequency homogenization for periodic media, Proc. R. Soc. Lond. 466 (2010) 2341–2362.
[24] T. Antonakakis, R.V. Craster, S. Guenneau, Homogenization for elastic photonic crystals and dynamic anisotropy, J. Mech. Phys. Solids 71 (2014) 84–96.
[25] C. Boutin, A. Rallu, S. Hans, Large scale modulation of high frequency waves in periodic elastic composites, J. Mech. Phys. Solids 70 (2014) 362–381.
[26] D.J. Colquitt, R.V. Craster, T. Antonakakis, S. Guenneau, Rayleigh–Bloch waves along elastic diffraction gratings, Proc. R. Soc. Lond. Ser. A Math. Phys. Eng. Sci. 471 (2173) (2014).
[27] F. Zolla, G. Renversez, A. Nicolet, B. Kuhlmey, S. Guenneau, D. Felbacq, Foundations of Photonic Crystal Fibres, Imperial College Press, London, 2005.
[28] S. Guenneau, A. Nicolet, F. Zolla, A finite element formulation for spectral problems in optical fibers, COMPEL 45 (1) (2001) 120–131.
[29] S. Guenneau, C.G. Poulton, A.B. Movchan, Oblique propagation of electromagnetic and elastic waves for an array of cylindrical fibres, Proc. R. Soc. Lond. Ser. A Math. Phys. Eng. Sci. 459 (2003) 2215–2263.
[30] R. Porter, D.V. Evans, Rayleigh-Bloch surface waves along periodic gratings and their connection with trapped modes in waveguides, J. Fluid Mech. 386 (1999) 233–258.
[31] D.S. Janning, B.A. Munk, Effects of surface waves on the currents of truncated periodic arrays, IEEE Trans. Antennas and Propagation 50 (9) (2002) 1254–1265.
[32] I. Thompson, C.M. Linton, Guided surface waves on one- and two-dimensional arrays of spheres, SIAM J. Appl. Math. 70 (8) (2010) 2975–2995.
[33] C.M. Linton, V. Zalipaev, I. Thompson, Electromagnetic guided waves on linear arrays of spheres, Wave Motion 50 (2013) 29–40.

[34] C.L. Holloway, D.C. Love, E.F. Kuester, J.A. Gordon, D.A. Hill, Use of generalized sheet transition conditions to model guided waves on metasurfaces/metafilms, IEEE Trans. Antennas and Propagation 60 (2012) 5173–5186.
[35] R.A. Shore, A.D. Yaghjian, Traveling waves on two- and three-dimensional periodic arrays of lossless scatterers, Radio Sci. 42 (2007) RS6S21.
[36] C.T. Chan, F. Huang, F. Liu, Z.H. Hang, Dirac dispersion and zero-index in two dimensional and three dimensional photon and phononic systems, Prog. Electromagnetics Res. B 44 (2012) 163–190.
[37] Y. Wu, J. Li, Q. Zhang, C.T. Chan, Effective medium theory for magnetodielectric composites: Beyond the long-wavelength limit, Phys. Rev. B 74 (085111) (2006).
[38] N.M. Litchinitser, A.K. Abeeluck, C. Headley, B.J. Eggleton, Antiresonant reflecting photonic crystal optical waveguides, Opt. Lett. 27 (18) (2002) 1592–1594.
[39] COMSOL Ltd. Comsol multiphysics 5.0, 2014.
[40] J.B. Pendry, L. Martín-Moreno, F.J. Garcia-Vidal, Mimicking surface plasmons with structured surfaces, Science (New York, N.Y.) 305 (5685) (2004) 847–848.
[41] C.M. Linton, R. Porter, I. Thompson, Scattering by a semi-infinite periodic array and the excitation of surface waves, SIAM J. Appl. Math. 67 (5) (2007) 1233–1258.
[42] R. Porter, D.V. Evans, Embedded RayleighBloch surface waves along periodic rectangular arrays, Wave Motion 43 (1) (2005) 29–50.
[43] S.A. Maier, S.R. Andrews, L. Martín-Moreno, F.J. García-Vidal, Terahertz surface plasmon-polariton propagation and focusing on periodically corrugated metal wires, Phys. Rev. Lett. 97 (17) (2006) 1–4.
[44] M. Navarro-Cía, M. Beruete, S. Agrafiotis, F. Falcone, M. Sorolla, S. Maier, Broadband spoof plasmons and subwavelength electromagnetic energy confinement on ultrathin metafilms, Opt. Express 17 (20) (2009) 18184–18195.
[45] D.J. Colquitt, I.S. Jones, N.V. Movchan, A.B. Movchan, Dynamic anisotropy and localization in elastic lattice systems, Waves Random Complex Media 22 (2) (2011) 1–17.
[46] R.V. Craster, T. Antonakakis, M. Makwana, S. Guenneau, Dangers of using the edges of the Brillouin zone, Phys. Rev. B 86 (11) (2012) 1–6.
[47] G.G. Osharovich, M.V. Ayzenberg-Stepanenko, O. Tsareva, Wave propagation in elastic lattices subjected to a local harmonic loading. II. Two-dimensional problems, Contin. Mech. Thermodyn. 22 (6–8) (2010) 599–616.
[48] A. Poddubny, I. Iorsh, P. Belov, Y. Kivshar, Hyperbolic metamaterials, Nat. Photonics 7 (12) (2013) 948–957.
[49] P. Shekhar, J. Atkinson, Z. Jacob, Hyperbolic metamaterials: fundamentals and applications, Nano Converg. 1 (1) (2014) 14.
[50] M. Makwana, A. Antonakakis, B. Maling, S. Guenneau, R.V. Craster, Wave mechanics in media pinned at Bravais lattice points, SIAM J. Appl. Math. 76 (2016) 1–26.
[51] M. Fernandez-Guasti, Green's second identity for vector fields, ISRN Math. Phys. 2012 (2012) 973968.